A priori study of subgrid-scale flux of a passive scalar in isotropic homogeneous turbulence

Sergei G. Chumakov*
Center for Nonlinear Studies and T-3, Computational Fluid Dynamics, Los Alamos National Laboratory, Los Alamos, New Mexico 87545, USA

(Received 21 April 2008; revised manuscript received 18 July 2008; published 15 September 2008)

We perform a direct numerical simulation (DNS) of forced homogeneous isotropic turbulence with a passive scalar that is forced by mean gradient. The DNS data are used to study the properties of subgrid-scale flux of a passive scalar in the framework of large eddy simulation (LES), such as alignment trends between the flux, resolved, and subgrid-scale flow structures. It is shown that the direction of the flux is strongly coupled with the subgrid-scale stress axes rather than the resolved flow quantities such as strain, vorticity, or scalar gradient. We derive an approximate transport equation for the subgrid-scale flux of a scalar and look at the relative importance of the terms in the transport equation. A particular form of LES tensor-viscosity model for the scalar flux is investigated, which includes the subgrid-scale stress. Effect of different models for the subgrid-scale stress on the model for the subgrid-scale flux is studied.

DOI: 10.1103/PhysRevE.78.036313 PACS number(s): 47.27.ep, 47.51.+a, 47.27.T−, 47.27.ek

I. INTRODUCTION

In the large eddy simulation (LES), the large-scale features of the flow are resolved directly and the effect of the unresolved, or subgrid scales (SGS) of motion is modeled [1]. The statistical information about behavior of the small-scale flow quantities is of great importance for it can be used to verify the assumptions of existing SGS models and provide constraints that have to be satisfied by the ones currently in development [2–4].

The LES transport equations are obtained by applying the spatial filter to the Navier-Stokes and scalar transport equations. The continuity equation does not change its form, the momentum and scalar transport equations become

$$\partial_t \bar{u}_i + \bar{u}_j \partial_j \bar{u}_i = -\partial_i P + \nu \partial_{jj}^2 \bar{u}_i - \partial_j \tau_{ij}, \tag{1}$$

$$\partial_t \bar{\phi} + \bar{u}_i \partial_i \bar{\phi} = \kappa \partial_{ii}^2 \bar{\phi} - \partial_i \tau_{i\phi}. \tag{2}$$

Here, $P=p/\rho$ is the modified pressure, $\nu=\mu/\rho$ is the kinematic viscosity, ϕ is the passive scalar, κ is the diffusion coefficient, $\bar{\phi}=\phi * G$ is the resolved part of ϕ, $\tau_{ij}=\overline{u_i u_j}-\bar{u}_i\bar{u}_j$ is the SGS stress, and $\tau_{i\phi}=\overline{u_i\phi}-\bar{u}_i\bar{\phi}$ is the SGS scalar flux. The latter two terms have to be modeled. In the rest of the paper, τ_ϕ will be used to denote the subgrid-scale flux, while $\tau_{i\phi}$ will denote its components.

While there exists a large body of work on modeling τ_{ij}, relatively few closures are developed for τ_ϕ that do not rely on simplifying assumptions (e.g., Kraichnan advection model [5]). The most popular models employ the eddy-viscosity approach [6,7],

$$\tau_{i\phi} \approx -(C_S\Delta)^2 |\bar{S}| \partial_i \bar{\phi}. \tag{3}$$

Here, Δ is the characteristic length of the LES filter (usually LES mesh size), $\bar{S}_{ij}=\frac{1}{2}(\partial_j \bar{u}_i+\partial_i \bar{u}_j)$ is the resolved rate-of-strain tensor, $|\bar{S}|=\sqrt{2\bar{S}_{ij}\bar{S}_{ij}}$ is its magnitude, and C_S is the Smagorinsky constant which can be prescribed *a priori* or determined dynamically via Germano identity using a least squares technique proposed by Lilly [8,9]. Although the dynamic determination of C_S seems to improve the result dramatically in comparison to constant C_S, it does not eliminate the major flaw of the model (3), which is the assumption that the gradient of the resolved scalar aligns well with the SGS scalar flux. This assumption, which rests on the molecular analogy, has been criticized by many, including Corrsin as early as in 1974 [10], and will be examined later in the paper.

A much better prediction is given by the scale-similarity model [11],

$$\tau_{i\phi} \approx C_{SS} L_{i\phi}, \quad L_{i\phi} = \widehat{\bar{u}_i\bar{\phi}} - \hat{\bar{u}}_i \hat{\bar{\phi}}. \tag{4}$$

Here, $L_{i\phi}$ is referred to as the Leonard term and is obtained using the so-called test filter, which has the characteristic length $\hat{\Delta}>\Delta$ and is applied to the LES (base-filtered) flow. The scaling constant C_{SS} is to be supplied by the user. Note that this model is Galilean invariant [12], as opposed to the earlier notations [13] where $L_{i\phi}$ could denote $\widehat{\bar{u}_i\bar{\phi}}-\bar{u}_i\bar{\phi}$.

The gradient viscosity, or Clark model [14]

$$\tau_{i\phi} \approx C_C \Delta^2 \partial_j \bar{u}_i \partial_j \bar{\phi}, \tag{5}$$

gives an excellent prediction in *a priori* tests, because it represents the first term in the Taylor series expansion for τ_ϕ [15]. Unfortunately, the Clark model has been shown to produce an effective negative diffusion for the case of incompressible flow, which potentially leads to a blowup in calculations [16]. This can be attributed to the fact that the deconvolution operator is unbounded in the natural function space for velocity and scalar fields, such as L^p [17].

The most straightforward way to avoid blowups is to augment the model (5) by the eddy viscosity term, resulting in a mixed model [18],

$$\tau_{i\phi} \approx C_C \Delta^2 \partial_j \bar{u}_i \partial_j \bar{\phi} - (C_S\Delta)^2 |\bar{S}| \partial_i \bar{\phi}. \tag{6}$$

Here, the value of C_C is usually set to $1/12$, and C_S is obtained using the Germano identity.

*chumakov@lanl.gov

TABLE I. DNS parameters.

Run name	N	ν	R_λ	η	ηk_{max}	Sc	Scalar forcing	Samples
512.20	512	1/2225	286	4.9×10^{-3}	1.19	1.0	mean gradient	100
512.21	512	1/1300	246	7.4×10^{-3}	1.78	1.0	mean gradient	100
1024.01	1024	1/4500	424	3.0×10^{-3}	1.40	1.0	mean gradient	106

A model that avoids user-specified constants is the dynamic structure (DS) model [19,20],

$$\tau_{i\phi} \approx \frac{\theta}{\Theta} L_{i\phi}. \tag{7}$$

Here, $\theta = \overline{\phi\phi} - \bar{\phi}\bar{\phi}$ is the SGS scalar variance, $\Theta = \widehat{\bar{\phi}\bar{\phi}} - \hat{\bar{\phi}}\hat{\bar{\phi}}$, and $L_{i\phi}$ is the Leonard term defined above. The model can be regarded as a scale-similarity model with particular scaling coefficient or can be derived using dynamic approach via Germano identity. Note that the SGS scalar variance is unavailable from the resolved field, which requires either a separate model or a separate transport equation for θ.

Lately, the progress in the measuring techniques and rapid advance in the computational power facilitated a growing interest in the *a priori* testing of the SGS models. In particular, one can judge the model performance by how well the model matches the topological characteristics of the modeled quantity such as eigenvalue configuration [20], or alignment trends with respect to the resolved flow structures such as principal strain directions, vorticity, and scalar gradient. Experimental data [4,21] and direct numerical simulation (DNS) [22] have been used to investigate and explain the misalignment of the principal axes of τ_{ij} and $\bar{S}_{ij}$.

Similar *a priori* tests based on experimental measurements have been performed for τ_ϕ. Higgins *et al.* [18] reports the alignment trends of τ_ϕ based on the measurements of temperature fluctuations in the atmospheric boundary layer. Their measurements indicate that the vectors τ_ϕ and $\nabla\bar{\phi}$ do not align, but the vectors τ_ϕ, $\nabla\bar{\phi}$, and the vector given by the Clark model (5) tend to be coplanar, thus supporting the argument about applicability of the mixed model. Sun and Su [23] use measurements of passive scalar in a cross-flowing jet to *a priori* test the eddy-viscosity, scale-similarity, mixed, and DS models for τ_ϕ. Their results indicate that DS and mixed models give comparable results that are superior to eddy-viscosity and scale-similarity models.

The goal of this work is to provide a detailed *a priori* analysis of the SGS passive scalar flux for the case of Schmidt number of unity. Based on the DNS results we will look at the relative importance of several terms in the transport equation for τ_ϕ. Also we will look at the behavior of τ_ϕ from the point of view of statistical geometry by evaluating *a priori* the characteristics such as alignment trends. In the end, a tensor-viscosity model for SGS flux based on the work by Daly and Harlow [24] is evaluated. Because this model uses the SGS stress to model the SGS flux, it is evaluated with two different SGS stress models.

II. DNS DESCRIPTION

The DNS parameters are summarized in Table I, the energy spectra are shown in Fig. 1. The incompressible Navier-Stokes equations were solved in a periodic box with sides of length $L=2\pi$ and N grid points in every direction. A standard pseudospectral algorithm was used, fully dealiased by a combination of spherical truncation and phase shifting [25]. The turbulence is sustained by a deterministic forcing term [26]

$$f_\alpha(\mathbf{k},t) = \begin{cases} \epsilon u_\alpha(\mathbf{k},t)/[2E_f(t)], & 0 < k < k_f, \\ 0, & k_f \leqslant k, \end{cases}$$

where ϵ is the mean dissipation rate and $E_f(t) = \int_0^{k_f} E(k,t)dk$, $E(k,t)$ is the energy spectrum at a given time. The mean dissipation rate ϵ was fixed at 0.12, and $k_f = 1.5$.

To resolve all important scales of motion, the condition $k_{max}\eta \geqslant 1$ was satisfied at all times in all simulations [27]. Here $k_{max} = N\sqrt{2}/3$ is the maximum significant wave number resolved by the grid, and η is the Kolmogorov length scale. The flow was initialized using velocity components with Gaussian distribution and random phases. Forcing was turned on and the flow was allowed to fully develop, after that the snapshots of the flow field were taken.

The consecutive snapshots should be separated far enough in time for the data to be temporally uncorrelated. In our database, the snapshots in 512^3 simulations are separated by slightly less than half of the eddy-turnover time τ_e, and in 1024^3 simulation by roughly $\tau_e/6$. For the purpose of this work, we took the snapshots that are about τ_e apart in time. Thus the results for 512^3 simulations are averaged over 50

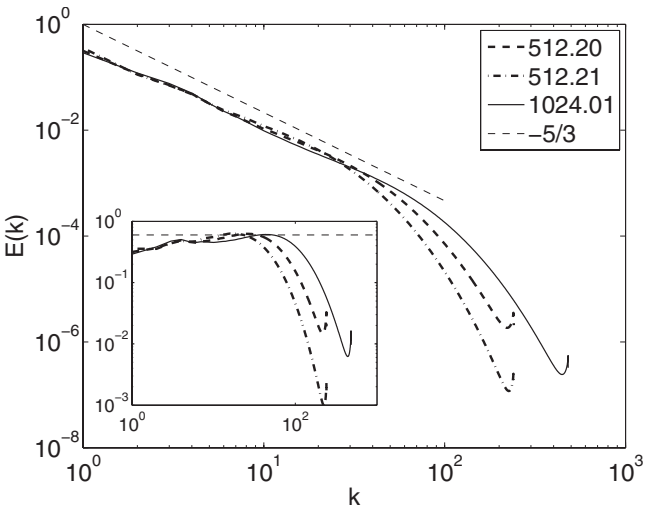

FIG. 1. Energy spectra of the three DNS runs from the Table I. The inset shows the same spectra compensated by $k^{5/3}$.

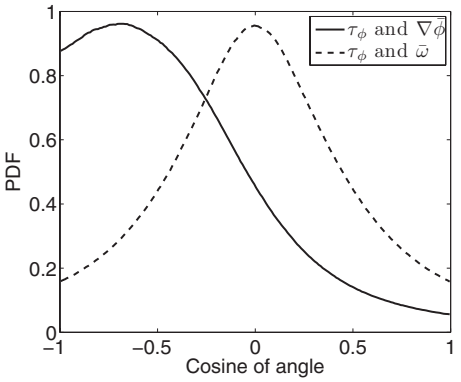

FIG. 2. PDF of cosine of angles between SGS scalar flux and resolved vector quantities: resolved scalar gradient $\nabla\bar{\phi}$ (solid) and resolved vorticity $\bar{\omega}$ (dashed). LES filter size $\Delta=0.2$.

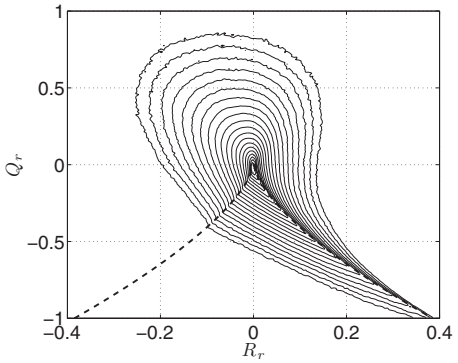

FIG. 3. Joint probability density function of (R_r, Q_r). LES filter size $\Delta=0.2$. Contours are logarithmically spaced from e^{-2} (outer) to 120.

snapshots, and results from the simulation 1024.01 over 17 snapshots.

It is known that in simulations of forced turbulence with mean scalar gradient it is sufficient to have $\eta k_{max} \geqslant 1.5$ for accurate prediction of the statistics that are second order and lower in small-scale scalar gradients [28,29]. Since we are mostly interested in the inertial-range scalar behavior, a simulation with $\eta k_{\max} \approx 1.2$ was also conducted to test the ability of slightly under-resolved simulations to capture the scalar behavior in the inertial range.

To obtain resolved and SGS quantities, Gaussian filters were applied with characteristic widths Δ logarithmically spaced from 0.05 to 1.6. In the figures, the data is taken from the run 512.21 unless stated otherwise.

III. DNS RESULTS AND DISCUSSION

Because the SGS scalar flux τ_ϕ is a vector, we will look at the probability density function (PDF) of the direction of τ_ϕ to gain more insight in the underlying physics, in the spirit of [18,30–33]. In particular, it is of interest to evaluate the alignment trends of τ_ϕ with respect to both resolved and subgrid structures.

It should be mentioned that in our *a priori* studies we assume that the implicit LES filter has a kernel that is positive in real space and close to Gaussian. Positiveness of the filter function ensures that τ_{ij} satisfies the realizability conditions [34]. The eigenvalues of τ_{ij} are non-negative and the SGS energy $k_s=\tau_{ii}/2$ is also non-negative, which ensures the applicability of our results to the eddy-viscosity models that use $\sqrt{k_s}$ as the characteristic SGS velocity [35–37].

A. Alignment of SGS flux and resolved structures

We denote by $\alpha(a,b)$ the angle between two vectors a and b. Figure 2 shows the PDF of $\cos\alpha(\tau_\phi,\nabla\bar{\phi})$ and $\cos\alpha(\tau_\phi,\bar{\omega})$, where $\bar{\omega}$ is resolved vorticity vector. It can be seen that resolved gradient and the SGS flux are not aligned, corroborating observation made by Corrsin [10] that gradient transport models might not work well in turbulence, where the size of the modeled phenomena is not larger than the "mean free path" by orders of magnitude. The misalignment of τ_ϕ and $\nabla\bar{\phi}$ was found to persist for all filter sizes (only one filter size is shown here) and the PDF of the angle between the two vectors seems not to depend on the filter size. The same can be said about the angle between τ_ϕ and $\bar{\omega}$.

To gain more information we conditioned the two cosines on the invariants of the resolved deformation rate tensor $\bar{A}_{ij}=\partial_j\bar{u}_i$, R_r and Q_r [38], the joint PDF of which is shown in Fig. 3. The dashed line is given by the zero discriminant $D=27R_r^2+4Q_r^3=0$. Below the dashed line, $\bar{A}_{ij}$ has no complex eigenvalues; above the dashed line $\bar{A}_{ij}$ has a pair of complex-conjugate eigenvalues $\lambda_{cr}\pm i\lambda_{ci}$, $\lambda_{ci}\geqslant 0$. We consider only the incompressible case here, thus the pair λ_{cr}, λ_{ci} fully determines the eigenvalue configuration of $\bar{A}_{ij}$. The ratio $s=\lambda_{ci}/\lambda_{cr}$ can be taken as a measure of "swirling intensity," similar to [39], where the reciprocal ratio $\lambda_{cr}/\lambda_{ci}$ is used. Isolines of the swirling intensity are shown in Fig. 4. In all figures, R_r is normalized by $\langle\bar{\omega}^2\rangle^{3/2}$, Q_r is normalized by $\langle\bar{\omega}^2\rangle$ (angle brackets denote the average over entire domain). The neighborhood of the right part of the dashed curve in the figures correspond to axisymmetric expansion (either without or with weak rotation)—the most frequent local flow state in homogeneous isotropic turbulence [40].

Figure 5 shows $\langle\cos\alpha(\tau_\phi,\nabla\bar{\phi})|(R_r,Q_r)\rangle$—the mean cosine of the angle between τ_ϕ and $\nabla\bar{\phi}$ conditioned on R_r and Q_r. The plot is truncated at the most outer contour of Fig. 3

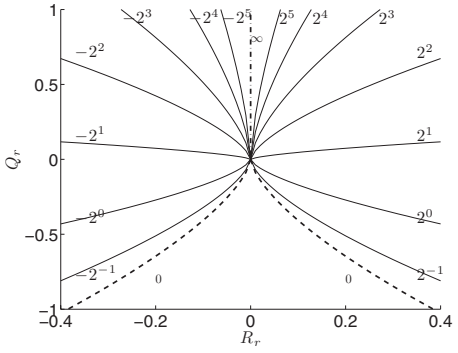

FIG. 4. Level lines of the swirling intensity $\lambda_{ci}/\lambda_{cr}$ in the (R,Q) plane. The dashed curve is given by $D=0$, the dashed-dotted curve is $-\infty$ on the left and $+\infty$ on the right.

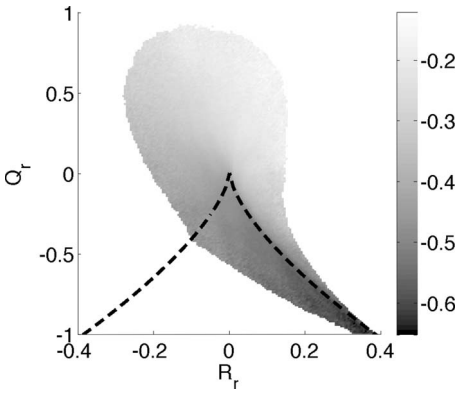

FIG. 5. Mean values of the cosine of angle between τ_ϕ and $\nabla\bar{\phi}$, conditioned on the invariants R_r and Q_r of the resolved deformation tensor $\partial\bar{u}_i/\partial x_j$. LES filter size $\Delta=0.2$.

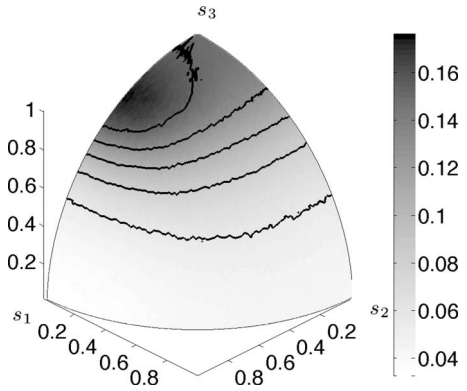

FIG. 7. Alignment trends of the SGS scalar flux in the resolved rate-of-strain eigenframe. LES filter size $\Delta=0.2$. Color represents the PDF.

in order to represent only the values of (R_r, Q_r) for which sufficient statistical samples were obtained. From Fig. 5 it is evident that in the strain-dominated areas that are close to axisymmetric expansion ($s<\delta$ for a small $\delta>0$, $R_r>0$) the SGS scalar flux τ_ϕ and resolved scalar gradient $\nabla\bar{\phi}$ are close to being counteraligned; while the alignment trends are less pronounced in the areas where the vorticity influence is not negligible ($|s|$ is not close to zero). This shows that the effective turbulent diffusion paradigm is applicable only in the strain-dominated areas. Note that the flow states along the right branch of the dashed curve are more frequent than the other states, which explains the ability of the countergradient models such as Eq. (3) to provide a feasible, however crude, average approximation to the SGS flux for large LES cell sizes.

The mean value of the cosine of angle between τ_ϕ and resolved vorticity $\bar{\omega}$ conditioned on (R_r, Q_r) are shown in Fig. 6. Together with the unconditioned PDF given in Fig. 2, it leads us to the conclusion that the angle between the resolved vorticity and SGS scalar flux does not heavily depend on the resolved flow configuration; the two vectors are approximately orthogonal, which supports the theory about the scalar sheetlike structures wrapped around the vortex tubes at small scales (see [41] and references therein). The only statistically significant departure from this trend happens when the swirling intensity is positive and not large, corresponding to a "weakly rotating unstable focus and/or compressing" configuration [38]. Apparently, the rotational effect in that configuration is not strong enough to produce a "sheet" of high scalar dissipation.

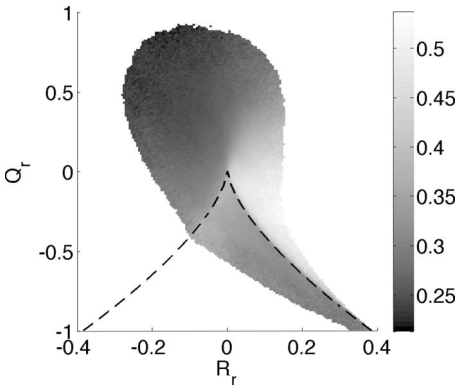

FIG. 6. Mean values of the absolute value of cosine of angle between τ_ϕ and $\bar{\omega}$, conditioned on the invariants R_r and Q_r of the resolved deformation tensor $\partial\bar{u}_i/\partial x_j$. LES filter size $\Delta=0.25$.

Also notable is the correlation between the swirling intensity levels in Fig. 4 and the cosine values in Figs. 5 and 6. This will be explored elsewhere.

The alignment of τ_ϕ in the basis defined by eigenvectors s_i of the resolved strain-rate tensor $\bar{S}_{ij}$ is shown in Fig. 7. The eigenvectors s_1, s_2, and s_3 correspond to the eigenvalues of the resolved strain, in the descending order: $\alpha\geqslant\beta\geqslant\gamma$. The alignment trend is nontrivial and does change visibly with the magnitude of local resolved enstrophy, which is demonstrated in Figs. 8 and 9. These figures show a persistent misalignment between τ_ϕ and $\nabla\bar{\phi}$ in the regions of high resolved enstrophy, while in the regions of low enstrophy τ_ϕ and $\nabla\bar{\phi}$ tend to be counteraligned.

Figure 10 shows the alignment trends between the resolved scalar gradient and the most compressive eigenvector of the resolved stress. It is evident that the directions of these two vectors coincide, regardless of the resolved enstrophy magnitude. A similar, although weaker, trend is shown in Fig. 11 between the intermediate eigenvector of $\bar{S}_{ij}$ and $\bar{\omega}$. The alignment trends from the figures do not seem to depend on the filter size. Other filter sizes (from $\Delta=0.05,\ldots,0.8$) were considered, resulting in similar plots (not shown). Thus, the classical result [30] about the alignment of vorticity, the scalar gradient strain axis also holds in the inertial range, e.g., the resolved vorticity tends to align with the intermediate resolved strain, while the resolved scalar gradient tends to align with the most compressive resolved strain.

Figures 7–10 imply that in the regions dominated by the large-scale strain, the SGS scalar flux is counteraligned with the resolved gradient, and both are aligned well with the most compressive direction of the resolved stress. Thus in low-enstrophy regions, the flux can be modeled using the eddy viscosity approach. In the vorticity-dominated areas, the countergradient assumption is not appropriate, since there is a persistent misalignment between the gradient and the

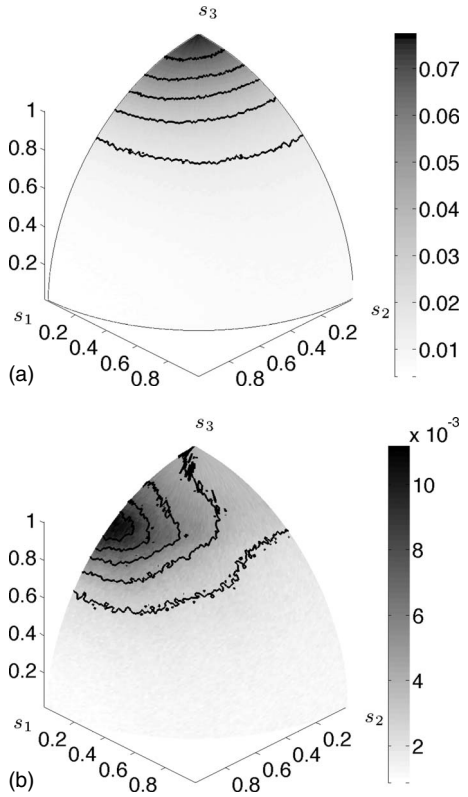

FIG. 8. Alignment trends of the SGS scalar flux in the resolved rate-of-strain eigenframe: dependence on the resolved enstrophy magnitude: (a) low, (b) high. LES filter size $\Delta=0.2$. Color represents the PDF.

flux. From Figs. 7 and 8 we conclude that the areas of misalignment compose the majority of our computational domain, since Figs. 7 and 8(b) are similar.

B. Alignment trends of SGS flux in the SGS stress eigenframe

Considering the alignment of τ_ϕ in the subgrid frame of reference, namely, the eigenframe of τ_{ij}, yields an interesting observation. The direction of τ_ϕ seems to nearly coincide with the direction of the most extensive eigenvector ξ_1 of the

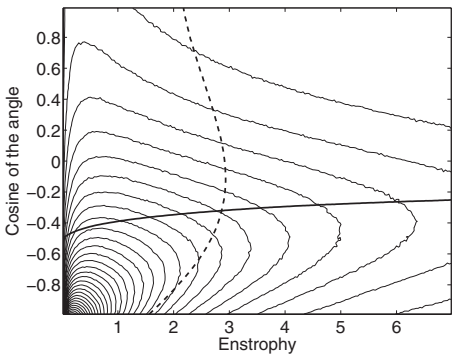

FIG. 9. Joint PDF of the resolved enstrophy $\bar{\omega}^2$ (normalized by its root mean square value) and the cosine of the angle between τ_ϕ and $\nabla\bar{\phi}$. Bold lines denote the conditional means. Contours are uniformly spaced between 0.01 and 0.45. $\Delta=0.2$.

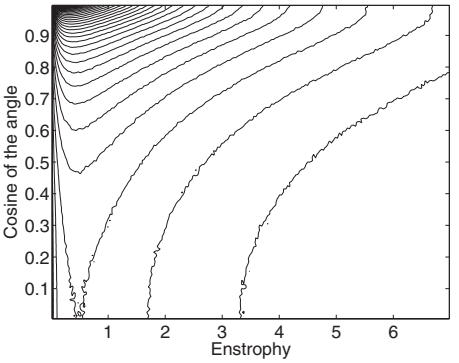

FIG. 10. Joint PDF of the resolved enstrophy $\bar{\omega}^2$ (normalized by its root mean square value) and the cosine of the angle between $\nabla\bar{\phi}$ and the most compressive eigenvector of $\bar{S}_{ij}$. Contours are uniformly spaced between 0.01 and 0.9. $\Delta=0.2$.

SGS stress τ_{ij}, which is illustrated in Figs. 12 and 13. This alignment, which persists regardless of the configurations of the resolved flow structures, explains quite complex dynamics of τ_ϕ with respect to the eigenframe of $\bar{S}_{ij}$ described in the previous section. The alignment dynamics between τ_{ij} and $\bar{S}_{ij}$ have been investigated *a priori* in a number of studies [4,21,22], but a qualitative explanation of the misalignment of the axis of τ_{ij} and $\bar{S}_{ij}$ has yet to appear. Now we look closer at the alignment of τ_ϕ and ξ_i.

In [3], we introduced two parameters s^* and q^*, each ranging between -1 and 1, to characterize the eigenvalue configuration of a symmetric matrix in a uniform fashion. Given a symmetric tensor B_{ij},

$$s^* = \frac{-\sqrt{6}\tilde{B}_{ii}^3}{(\tilde{B}_{jj}^2)^{3/2}},$$

$$q^* = \frac{1}{3\pi}[6\sin^{-1}W + 2W(5-2W^2)\sqrt{1-W^2}],$$

where $B_{ii}^2 = B_{ij}B_{ji}$, $B_{ii}^3 = B_{ij}B_{jk}B_{ki}$, $W = B_{ii}/\sqrt{3B_{jj}^2}$, and $\tilde{B}_{ij} = B_{ij} - \delta_{ij}B_{kk}/3$.

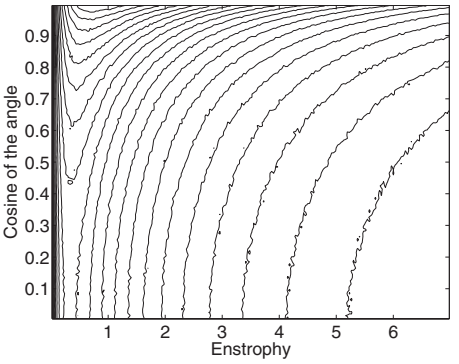

FIG. 11. Joint PDF of the resolved enstrophy $\bar{\omega}^2$ (normalized by its root mean square value) and the cosine of the angle between $\bar{\omega}$ and the intermediate eigenvector of $\bar{S}_{ij}$. Contours are uniformly spaced between 0.02 and 0.3. $\Delta=0.2$.

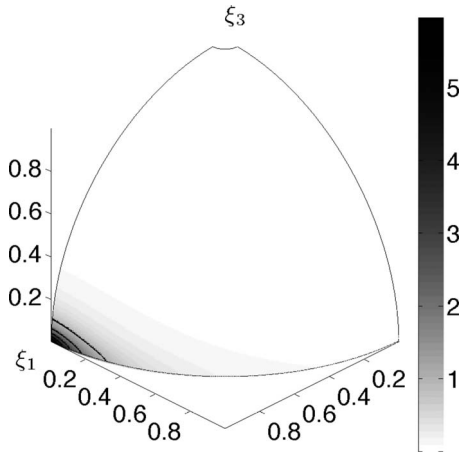

FIG. 12. Alignment trends of the SGS scalar flux in the SGS stress eigenframe. Run 512.21, $\Delta=0.05$. Color represents the PDF.

Applied to τ_{ij}, s_τ^* characterizes the relative position of the intermediate eigenvalue, while q_τ^* characterizes the importance of the isotropic part of τ_{ij}. In this work, Gaussian filters are employed as base LES filters, which results in nonnegative eigenvalues of τ_{ij}. This implies that for a given value of s_τ^*, there exists $q_{\mathrm{crit}}^*(s_\tau^*)>0$ such that $q_{\mathrm{crit}}^*(s_\tau^*)\leqslant q_\tau^* \leqslant 1$, where $q_{\mathrm{crit}}^*(s^*)$ can be found analytically by setting the smallest eigenvalue of τ_{ij} equal to zero. Thus $q_\tau^*=1$ when τ_{ij} is isotropic (all eigenvalues coincide) and $q_\tau^*=q_{\mathrm{crit}}^*(s_\tau^*)<1$ when τ_{ij} is singular [3].

Figure 14 shows the means of cosine of the angle between τ_ϕ and ξ_1 conditioned on the "relative q_τ^*" value

$$q_{\mathrm{rel}}^*(s_\tau^*,q_\tau^*) \equiv \frac{q_\tau^* - q_{\mathrm{crit}}^*(s_\tau^*)}{1-q_{\mathrm{crit}}^*(s_\tau^*)},$$

which is bounded by 0 and 1.

Figure 14 shows that regions with low q_{rel}^* (highly anisotropic τ_{ij}) correspond to very good alignment between τ_ϕ and ξ_1. On the other hand, when $q_{\mathrm{rel}}^*=1$, which is equivalent to

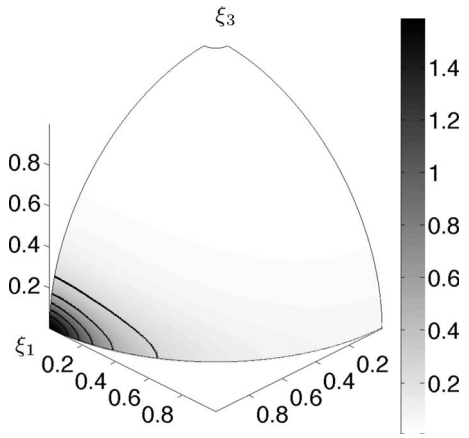

FIG. 13. Alignment trends of the SGS scalar flux in the SGS stress eigenframe. Run 512.21, $\Delta=0.8$. Color represents the PDF.

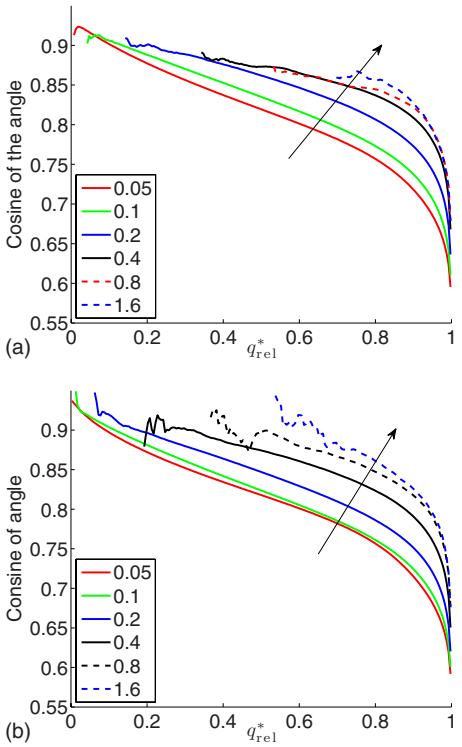

FIG. 14. (Color online) Cosine of the angle between the SGS scalar flux and the most extensive direction of the SGS stress, conditioned on q_{rel}^*. Legend refers to the sizes of the LES filter. Data sets (a) 512.20 and (b) 512.21. The arrows indicate the filter growth.

$q^*=1$ or isotropic τ_{ij}, the angle between τ_ϕ and ξ_1 seems to go to a universal value.

Let us denote by λ_i the eigenvalues of τ_{ij} and by $\tilde{\lambda}_i$ the eigenvalues of τ_{ij} normalized so that $\tau_{ii}^2=1$ (or, equivalently, $\tilde{\lambda}_i=\lambda_i/\sqrt{\lambda_j\lambda_j}$). Assume that $\tilde{\lambda}_1\geqslant\tilde{\lambda}_2\geqslant\tilde{\lambda}_3$, then $1/\sqrt{3}\leqslant\tilde{\lambda}_1\leqslant 1$, $0\leqslant\tilde{\lambda}_2\leqslant 1/\sqrt{2}$, and $0\leqslant\tilde{\lambda}_3\leqslant 1/\sqrt{3}$. We can find the mean value of the cosine of the angle between the directions of τ_ϕ and ξ_i, conditioned on $\tilde{\lambda}_i$. Such PDFs for two values of Δ from the inertial range are shown in Figs. 15 and 16. For each filter size, there are three PDFs plotted, one for each $\tilde{\lambda}_i$.

The most striking feature of the conditional PDFs is the closeness of the correlation between $\tilde{\lambda}_i$ and $|\cos\alpha(\tau_\phi,\xi_i)|$ to linear. This implies that in the eigenframe of τ_{ij}, the direction of the SGS flux nearly coincides with one of the eight directions that are given by the vectors $(\pm\tilde{\lambda}_1,\pm\tilde{\lambda}_2,\pm\tilde{\lambda}_3)$. Distribution of the largest normalized eigenvalue $\tilde{\lambda}_1$ is shown in Fig. 17. It can be seen that even for the largest filter considered ($\Delta=0.8$) the distribution peaks at values of $\tilde{\lambda}_1$ close to 1.

Given the correlation in Figs. 15 and 16, and the PDF from Fig. 17, the alignment between τ_ϕ and ξ_1 shown in Figs. 12 and 14 can indeed be expected. This alignment appears to be insensitive to the filter size. Other filter sizes (not shown) produced figures very similar to Fig. 15.

Figures 14 and 15 show results from different simulations: 512.20 and 512.21. The simulations differ in resolution, yet the statistics of the alignment trends are very

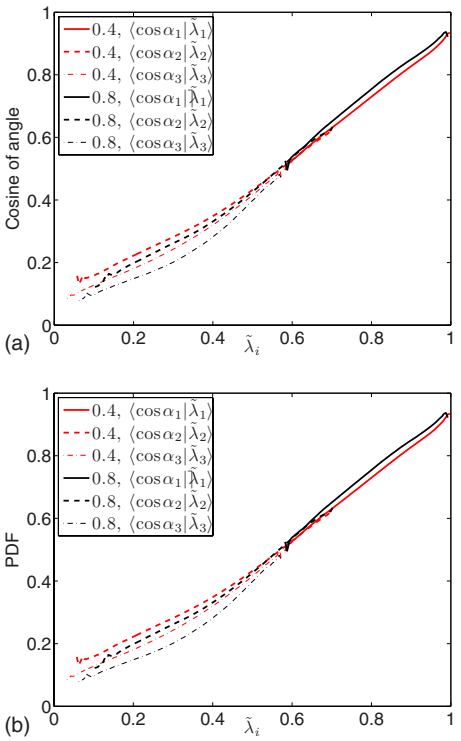

FIG. 15. (Color online) Cosine of the angles α_i between directions of the SGS scalar flux τ_ϕ and eigenvectors ξ_i of τ_{ij}, conditioned on the corresponding normalized eigenvalue $\tilde{\lambda}_i$, $i=1,2,3$. Data sets (a) 512.20, (b) 512.21.

close. This demonstrates that (at least for the case $Sc=1$) the simulation with $\eta k_{\max}=1.2$ shows similar structure of the coupled velocity-scalar field in the inertial range of scales.

IV. TRANSPORT EQUATION FOR THE SGS SCALAR FLUX

A. Derivation

To derive the transport equation for τ_ϕ, we start with the unfiltered momentum transport equation, multiply it by ϕ, add to the unfiltered scalar transport equation multiplied by u_i, and apply the filtering operation. The result is the transport equation for $\overline{u_i\phi}$. Using similar procedure, starting with (1) and (2) we obtain the transport equation for $\bar{u}_i\bar{\phi}$. Subtracting one resulting equation from the other, we obtain the following:

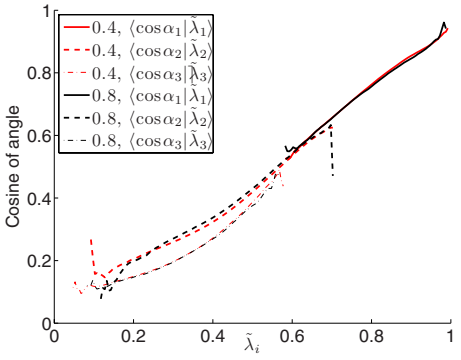

FIG. 16. (Color online) Same as in Fig. 15, but for 1024.01.

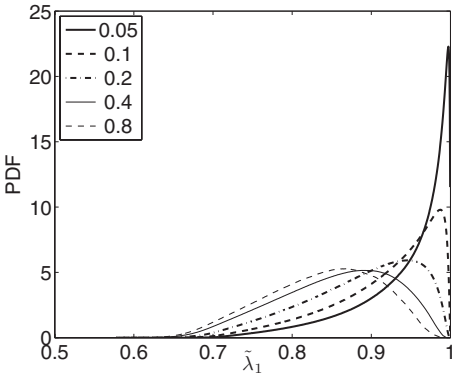

FIG. 17. The distribution of $\tilde{\lambda}_1$, the largest normalized eigenvalue of the SGS stress τ_{ij}. Legend corresponds to the filter size.

$$\partial_t\tau_{i\phi}+\bar{u}_j\partial_j\tau_{i\phi}=-\tau(\phi,\partial_i P)+\kappa\tau(u_i,\partial_{jj}\phi)+\nu\tau(\phi,\partial_{jj}u_i)-\tau(u_j,\partial_j(u_i\phi))+\bar{u}_i\partial_j\tau_{j\phi}+\bar{\phi}\partial_j\tau_{ij}. \quad (8)$$

Here, for brevity, we used the Germano [12] notations $\tau(a,b)=\overline{ab}-\bar{a}\bar{b}$.

The right-hand side (RHS) of Eq. (8) has six terms. The first term $D_P\equiv\tau(\phi,\partial_i P)$ is the scattering of the scalar by the subgrid pressure effects, which we are going to neglect for the purposes of this work. The diffusion terms (the second and third terms) can be combined in various ways. A possible combination is

$$D_{i\phi}=m\partial_{jj}\tau_{i\phi}-2m\tau(\partial_j u_i,\partial_j\phi)+(M-m)C, \quad (9)$$

where

$$m=\min(\kappa,\nu),\quad M=\max(\kappa,\nu),$$

$$C=\begin{cases}\tau(u_i,\partial_{jj}\phi), & \kappa>\nu,(Sc<1),\\ 0, & \kappa=\nu,(Sc=1),\\ \tau(\phi,\partial_{jj}u_i), & \kappa<\nu,(Sc>1).\end{cases}$$

The last three terms in Eq. (8) are source and sink terms. Using the Taylor expansion formula developed in [13,15] and the procedure outlined in [19], we can rewrite these terms, disregarding the entries of the third order in Δ and higher. This results in the following transport equation for $\tau_{i\phi}$:

$$\partial_t\tau_{i\phi}+\bar{u}_j\partial_j\tau_{i\phi}=-D_P+D_{i\phi}-\tau_{j\phi}\partial_j\bar{u}_i-\tau_{ij}\partial_j\bar{\phi}, \quad (10)$$

where $D_{i\phi}$ is given by Eq. (9). In this form, the source terms represent the creation and destruction of τ_ϕ by the action of the resolved deformation tensor $\bar{A}_{ij}$ on τ_ϕ, and action of the SGS stress τ_{ij} on the resolved scalar gradient $\nabla\bar{\phi}$.

We investigate the relative importance of the terms on the RHS of Eq. (10) using available DNS. In this work we restrict our investigations to the case $Sc=1$. This simplifies Eq. (10) to

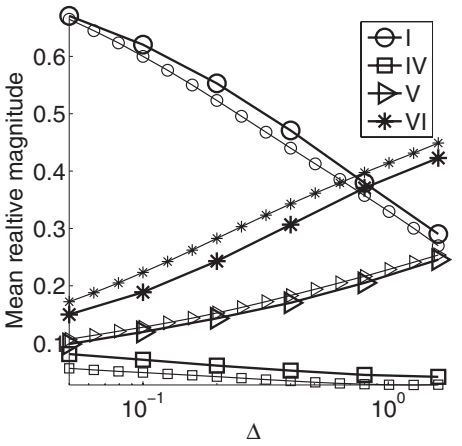

FIG. 18. Mean relative magnitudes of the terms I, IV, V, and VI. Dependence on the filter size. Thick lines show data from the run 512.21, thin lines show data from 1024.01.

$$\partial_t \tau_{i\phi} + \underbrace{\bar{u}_j \partial_j \tau_{i\phi}}_{I} = \underbrace{\kappa \partial_{jj} \tau_{i\phi}}_{II} - \underbrace{(\overline{\phi \partial_i P} - \bar{\phi} \partial_i \bar{P})}_{III} - \underbrace{2\kappa(\overline{\partial_j u_i \partial_j \phi} - \partial_j \bar{u}_i \partial_j \bar{\phi})}_{IV} - \underbrace{\tau_{j\phi} \partial_j \bar{u}_i}_{V} - \underbrace{\tau_{ij} \partial_j \bar{\phi}}_{VI}. \quad (11)$$

B. Relative importance of the terms

We assume that we can neglect the effects of pressure and diffusion. Thus we concentrate only on the terms I, IV, V, and VI in Eq. (11), which respectively represent convection, unresolved gradients' interaction, deformation of the SGS flux by the resolved flow structures, and effect of the SGS stress on the resolved scalar gradient. To estimate how the relative magnitude of these terms changes with the filter size, we plot the magnitude of these terms, normalized by the sum of their magnitudes, in Fig. 18.

It is evident from the figure that the term IV is insignificant and can be discarded for the modeling purposes.

The convective term is clearly dominant when Δ is close to the dissipative scale, thus supporting the hypothesis of "sweeping by large eddies" (see [42] and references therein). The sweeping effect weakens with the growth of the filter. The other two terms, V and VI, are of the same order of magnitude, with VI being about twice as large as V. The term VI becomes dominant at the upper end of the inertial range. The Reynolds number effect is also apparent: with increasing R_λ the role of the convective term I is diminishing for all filter sizes, while the source terms V and VI grow in magnitude. It is worth noting that we do not see any plateau in the inertial range.

V. MODELING THE SGS FLUX

A. A tensor viscosity model

The order-of-magnitude analysis in the previous section shows that the assumptions made by Daly and Harlow [24] are reasonably valid for the locally-averaged flows and the model

$$\tau_{i\phi} \approx \tau_{i\phi}^{\mathrm{mod}} \equiv -\frac{1}{|\bar{S}|} \tau_{ij} \partial_j \bar{\phi} \quad (12)$$

might give a good approximation for τ_ϕ. One can also include the other dominant term (V) in the modeling [43], or use it as a first approximation in the expansion of tensor viscosity [44]. The distribution of the cosine of angle between τ_ϕ^{mod} and τ_ϕ is given in Fig. 19 and the PDF of relative error in the magnitude $E=(|\tau_\phi^{\mathrm{mod}}|-|\tau_\phi|)/|\tau_\phi|$ is shown in Fig. 20.

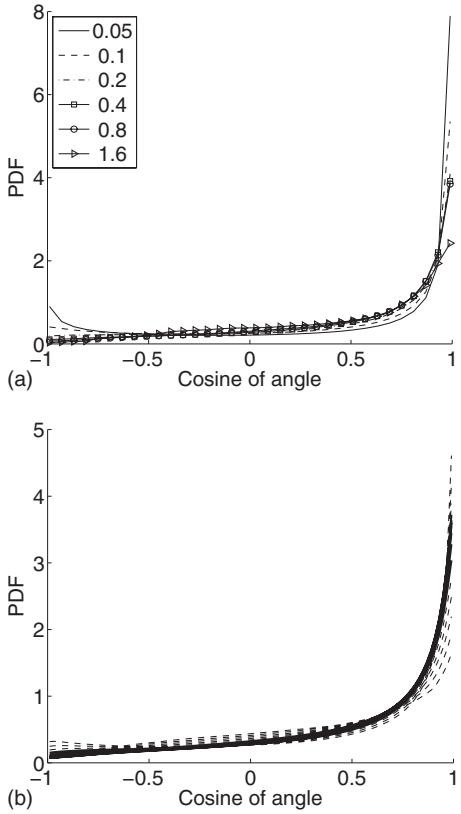

FIG. 19. Distribution of the cosine of the angle between the SGS flux and the model (12), tested on the data sets (a) 512.21 and (b) 1024.01. Different curves correspond to $\Delta=0.05,\ldots,1.6$. For clarity, in (b) the curves corresponding to the inertial range $\Delta=0.1,\ldots,0.5$ are bold.

The model (12) predicts the direction of the flux with reasonable accuracy, although for the smallest filter sizes (order of magnitude of η) a counteralignment with the flux can occur. In the inertial range ($\Delta=0.4,0.8$) the PDF seems to reach some asymptotic state. The PDF of the relative error in the magnitude of the flux also collapses in the inertial range, which is shown by solid lines.

The time scale $1/|\bar{S}|$ is taken from the resolved flow, and it gives a consistent magnitude of the flux, as opposed to SGS time scale $\Delta/\sqrt{k_s}$ that was also tested (not shown). Since k_s contains information from all subgrid scales, and $|\bar{S}|$ is a feature of the length scales close to Δ, it shows, in our opin-

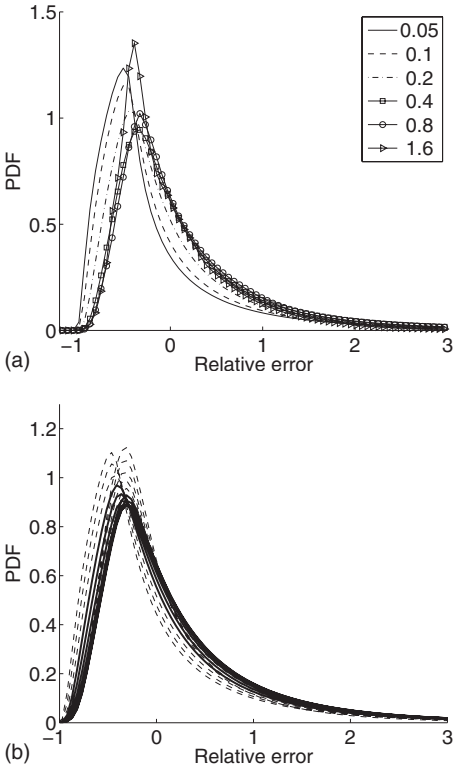

FIG. 20. Relative error of the model (12), tested on the datastets (a) 512.21 amd (b) 1024.01. Different curves correspond to $\Delta=0.05,\ldots,1.6$. For clarity, in (b) the curves corresponding to the inertial range $\Delta=0.1\ldots0.5$ are bold.

ion, that the dominant portion of the SGS scalar flux comes from the scales (in both scalar and velocity fields) that are close to Δ, which illustrates the locality of the cascade [45] for the case of a passive scalar.

Also the model (12) does not require any additional transport equations or operations; it relies on the quality of the model for the SGS stress τ_{ij}.

B. Dependence on the SGS stress model

To provide a comprehensive study, we conduct *a priori* tests of the model (12) with two different models for τ_{ij}: (1) the Smagorinsky model [27,46]

$$\tau_{ij}^{*} \approx -2(C_S\Delta)^2|\bar{S}|\bar{S}_{ij}, \quad C_S=0.18,$$

(2) the dynamic structure model [20,47]

$$\tau_{ij} \approx \frac{\tau_{mm}}{L_{nn}}L_{ij}, \quad L_{ij}=\widehat{\bar{u}_i\bar{u}_j}-\hat{\bar{u}}_i\hat{\bar{u}}_j.$$

Here, $\tau_{ij}^{*}=\tau_{ij}-\delta_{ij}\tau_{kk}/3$ is the deviatoric part of the SGS stress and "$\hat{\ }$" denotes the test filtering with the characteristic width $\hat{\Delta}=2\Delta$.

This results in two models for the SGS flux:

$$\tau_{i\phi} \approx -\frac{1}{|\bar{S}|}\tau_{ij}^{*}\partial_j\bar{\phi} \approx C_1 2(C_S\Delta)^2\bar{S}_{ij}\partial_j\bar{\phi}, \tag{13}$$

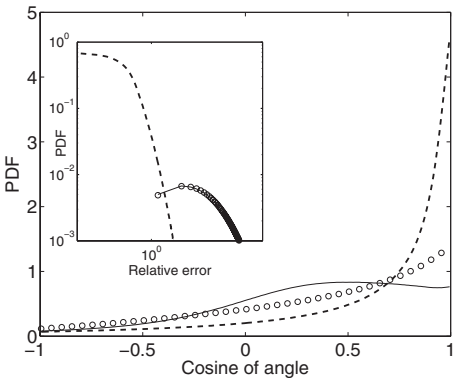

FIG. 21. Performance of the Smagorinsky-based model for τ_{ϕ}. The solid lines correspond to the full Smagorinsky model, the dashed lines to the deviatoric part, and the circles to the Smagorinsky model with the real trace of τ_{ij} added. The filter size $\Delta=0.2$.

$$\tau_{i\phi} \approx -\frac{1}{|\bar{S}|}\frac{2k_s}{L_{nn}}L_{ij}\partial_j\bar{\phi}. \tag{14}$$

The advantage of the model (13) is smaller computational overhead, while Eq. (14) does not have user-specified constants.

Note that in Eq. (13) we use the model only for the deviatoric part of the stress. Addition of trace results in severe degradation of the model's performance, as shown in Fig. 21 which depicts PDF of the cosine of the angle between τ_{ϕ} and the model and the magnitude of the relative error. The solid lines correspond to the model (12) with full Smagorinsky model $\tau_{ij}=-2(C_S\Delta)^2|\bar{S}|\bar{S}_{ij}+\delta_{ij}\tau_{kk}/3$, dashed lines correspond to the model (13), and the circles correspond to the composite model that has the trace of τ_{ij} found *a priori* and added to the Smagorinsky model for τ_{ij}^{*}. It can be seen that the addition of the trace degrades the performance of the model significantly, especially the prediction of the magnitude of the flux.

For models (13) and (14), the resulting PDFs of the angle between models and τ_{ϕ} and the relative error in the magnitude prediction are shown in Fig. 22 for $\Delta=0.2$. The other filter sizes produce similar plots; the means of the PDFs of relative error are shown in Table II for different filter sizes.

Surprisingly, the model (13), based on the deviatoric part of the Smagorinsky model with $C_1=2$, gives the most accurate prediction for the flux direction for all filter sizes, outperforming model (12) which has the "ideal" SGS stress.

Model (14) gives the distributions of angle and relative error which are close to the "ideal" model (12), which corroborates the earlier findings about the good quality of the dynamic structure model itself.

Overall these figures show that *a priori* the simplest tensor-viscosity approach can very well predict the direction of the flux while the accurate prediction of the magnitude may either require some higher-order corrections [44] or a different approach, such as scale similarity. However, if we directly incorporate the model (13) in the LES equations (2), the following term appears in the right-hand side of the transport equation: $\bar{S}_{ij}\partial_{ij}^2\bar{\phi}$. This, similarly to the Clark

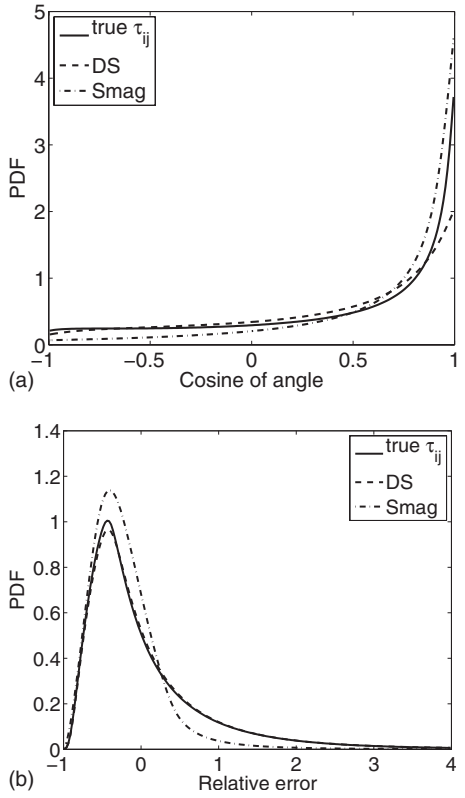

FIG. 22. (a) Angle between τ_ϕ and models (12) and (13) with $C_1=2$ and (14). (b) Relative error of the models (12) and (13) with $C_1=2$ and (14). The filter size $\Delta=0.2$.

model, gives effectively negative diffusion [16], which, if unchecked, might lead to a blowup in the LES calculations. The *a posteriori* stability of this model is outside of the scope of the present paper and will be investigated in future work.

VI. CONCLUSIONS

We performed several DNS runs of forced homogeneous isotropic turbulence with passive scalar, which is forced by mean gradient, with $Sc=1$ and different degree of resolution ($\eta k_{\max}=1.2, 1.4, 1.78$). The DNS data was used to investigate *a priori* the alignment trends of the SGS scalar flux for various LES filter sizes ranging from several Kolmogorov scales to forcing scale. Some persistent alignment trends between the SGS flux and resolved flow structures were found, but they were observed to depend on many parameters. We found that the degree of resolution in all our DNS runs was sufficient to resolve the inertial-range statistical geometry trends.

TABLE II. Mean values of the relative error for models (12) (True), (13) with $C_1=2$ (Smag), and (14) (DS), dependence on the filter size.

Δ	True	Smag	DS
0.05	−0.13	0.07	−0.165
0.1	−0.05	−0.05	−0.07
0.2	0.10	−0.19	0.10
0.4	0.20	−0.33	0.25

Our results show that the effective turbulent viscosity approach is applicable only in strain-dominated (low-enstrophy) areas of the flow. Because the strain-dominated states are the most frequent in turbulent flow, as the joint PDF of (R_r, Q_r) shows, the effective turbulent viscosity approach gives a feasible engineering approximation, although it is physically inconsistent.

It was found that the direction of the SGS scalar flux was strongly connected with the eigenvectors and eigenvalues of the SGS stress τ_{ij}. In particular, the mean cosine of the angle between the flux τ_ϕ and an eigenvector ξ_i of τ_{ij} was found to be highly correlated with the relative magnitude of the corresponding eigenvalue $\tilde{\lambda}_i$; the correlation was found to be close to linear. This, together with the calculated PDF for the normalized largest eigenvalue of τ_{ij}, leads us to the conclusion that the SGS flux is in general closely aligned with the maximum eigenvector of τ_{ij}.

We derived an approximate transport equation for the scalar flux and looked at the relative importance of the transport, source, and sink terms. We found that convective effects dominate in the near-viscous range, while in the inertial range the dominant term represents the work of the SGS stress τ_{ij} on the resolved scalar gradient, which shows applicability to LES of the Reynolds-Averaged Navier-Stokes (RANS) model proposed by Daly and Harlow [24].

We evaluated a model analogous to the one proposed by Daly and Harlow using our DNS data and found that it gave good prediction for the SGS scalar flux in the inertial range of LES filters; both in terms of direction and magnitude of the SGS flux vector. The time scale that gave the correct flux magnitude was based on the resolved strain as opposed to the SGS kinetic energy. This shows that the dominant portion of the SGS scalar flux comes from the scales that are close to the characteristic LES filter size, which is coherent with the locality of the cascade [45]. The model has an advantage of not requiring any additional transport equations or additional filtering, it does not have any user-adjustable constants. Thus for incompressible flows with passive scalars, the quality of modeling of the SGS stress τ_{ij} becomes the primary concern.

We evaluated the effect of two different models for τ_{ij} on the quality of prediction for τ_ϕ: the Smagorinsky model and dynamic structure (DS) model. The prediction quality of the DS model appeared to be consistent with earlier studies. However, the utilization of the traceless part of the Smagorinsky model gave an unexpectedly good prediction for the direction of the flux, while the reasonable prediction of the magnitude required an additional user-specified constant. Inclusion of trace of τ_{ij}—either isotropic or *a priori* calculated—led to degradation in the model performance. It is worth noting that the application of this particular tensor-viscosity model (deviatoric part of the Smagorinsky model) in *a posteriori* calculations can potentially lead to instabilities due to effective negative viscosity provided by a part of the model, similar to [16], however, the negative viscosity might be counteracted by the other part of the model. A more

thorough investigation of this modeling issue will be conduced in future work.

ACKNOWLEDGMENTS

The author is indebted to C. J. Rutland, R. Rubinstein, C. Meneveau, and R. Rauenzahn for stimulating discussions, and to anonymous reviewers for valuable comments. The computations were performed using the computational resources at Center for Nonlinear Studies and various Linux clusters at LANL via Institutional Computing Grant. This work was performed under auspices of the US Department of Energy (Contract No. W-7405-ENG).

[1] P. Sagaut, *Large Eddy Simulation for Incompressible Flows: An Introduction* (Springer-Verlag, Berlin, 2006).
[2] S. Cerutti and C. Meneveau, Phys. Fluids **10**, 928 (1998).
[3] S. G. Chumakov, J. Fluid Mech. **562**, 405 (2006).
[4] B. Tao, J. Katz, and C. Meneveau, J. Fluid Mech. **547**, 35 (2002).
[5] A. Celani, M. Martins Alfonso, and A. Mazzino, J. Turbul. **7**, 1 (2006).
[6] P. Moin, K. Squires, W. Cabot, and S. Lee, Phys. Fluids A **3**, 2746 (1991).
[7] C. D. Pierce and P. Moin, J. Fluid Mech. **504**, 73 (2004).
[8] M. Germano, U. Piomelli, P. Moin, and W. H. Cabot, Phys. Fluids A **3**, 1760 (1991).
[9] D. K. Lilly, Phys. Fluids A **4**, 633 (1992).
[10] S. Corrsin, Adv. Geophys. **18**, 25 (1974).
[11] J. Bardina, J. H. Ferziger, and W. C. Reynolds, AIAA Pap. **80**, 1357 (1980).
[12] M. Germano, J. Fluid Mech. **238**, 325 (1992).
[13] A. Leonard, Adv. Geophys. **18**, 237 (1974).
[14] R. A. Clark, J. H. Ferziger, and W. C. Reynolds, J. Fluid Mech. **91**, 1 (1979).
[15] W. Yeo and K. Bedford, *Computational Methods in Flow Analysis*, edited by H. Niki and M. Kawahara (Okayama University of Science, Okayama, 1988), pp. 844–851.
[16] A. Leonard, AIAA Pap. **1997**, 204 (1997).
[17] G. L. Eyink, J. Fluid Mech. **549**, 159 (2006).
[18] C. Higgins, M. Parlange, and C. Meneveau, Geophys. Res. Lett. **31**, L22105 (2004).
[19] S. G. Chumakov and C. J. Rutland, AIAA J. **42**, 1132 (2004).
[20] S. G. Chumakov and C. J. Rutland, Int. J. Numer. Methods Fluids **47**, 911 (2005).
[21] H. S. Kang and C. Meneveau, Phys. Fluids **17**, 055103 (2005).
[22] K. Horiuti, J. Fluid Mech. **491**, 65 (2003).
[23] O. Sun and L. Su, AIAA Pap. **2004**, 2550 (2004).
[24] B. J. Daly and F. H. Harlow, Phys. Fluids **13**, 2634 (1970).
[25] C. Canuto, M. Hussaini, A. Quarteroni, and T. Zang, *Spectral Methods in Fluid Dynamics* (Springer, Berlin, 1988).
[26] L. Machiels, Phys. Rev. Lett. **79**, 3411 (1997).
[27] S. B. Pope, *Turbulent flows* (Cambridge University Press, Cambridge, 2000).
[28] A. Pumir, Phys. Fluids **6**, 2118 (1994).
[29] P. Vedula, P. K. Yeung, and R. O. Fox, J. Fluid Mech. **433**, 29 (2001).
[30] W. T. Ashurst, A. R. Kerstein, R. M. Kerr, and C. H. Gibson, Phys. Fluids **30**, 2343 (1987).
[31] C. W. Higgins, M. B. Parlange, and C. Meneveau, Boundary-Layer Meteorol. **109**, 58 (2003).
[32] K. K. Nomura and P. J. Diamessis, Phys. Fluids **12**, 846 (2000).
[33] K. K. Nomura and G. K. Post, J. Fluid Mech. **377**, 65 (1998).
[34] B. Vreman, B. Geurts, and H. Kuerten, J. Fluid Mech. **278**, 351 (1994).
[35] S. Ghosal, T. S. Lund, P. Moin, and K. Akselvoll, J. Fluid Mech. **286**, 229 (1994).
[36] W. Kim and S. Menon, AIAA Pap. **95**, 0356 (1995).
[37] A. Yoshizawa and K. Horiuti, J. Phys. Soc. Jpn. **54**, 2834 (1985).
[38] M. Chong, A. Perry, and B. Cantwell, Phys. Fluids A **2**, 765 (1990).
[39] P. Chakraborty, S. Balachandar, and R. J. Aadrian, J. Fluid Mech. **535**, 189 (2005).
[40] T. S. Lund and M. M. Rogers, Phys. Fluids **6**, 1838 (1994).
[41] R. A. Antonia and P. Orlandi, Appl. Mech. Rev. **56**, 615 (2003).
[42] M. Nelkin and M. Tabor, Phys. Fluids A **2**, 81 (1990).
[43] S.-H. Peng and L. Davidson, Int. J. Heat Mass Transfer **45**, 1393 (2002).
[44] B. C. Wang, E. Yee, D. Bergstrom, and O. Iida, J. Fluid Mech. **604**, 125 (2008).
[45] G. L. Eyink, Physica D **207**, 91 (2005).
[46] J. Smagorinsky, Mon. Weather Rev. **91**, 99 (1963).
[47] E. Pomraning and C. J. Rutland, AIAA J. **40**, 689 (2002).